Optically Beamformed Beam-Switched Adaptive Antennas for Fixed and Mobile Broad-Band Wireless Access Networks

Miguel A. Piqueras, Gerd Grosskopf, Borja Vidal, Javier Herrera, Jose Manuel Martínez, Pablo Sanchis, Valentín Polo, Juan. L. Corral, Alexandre Marceaux, Julien Galière, Jérôme Lopez, Alain Enard, Jean-Luc Valard, Olivier Parillaud, Eric Estèbe, Nakita Vodjdani, Moon-Soon Choi, Jan Hendrik den Besten, Francisco M. Soares, Meint K. Smit, and Javier Marti

Invited Paper

***Abstract*—In this paper, a 3-bit optical beamforming architecture based in 2×2 optical switches and dispersive media is proposed and demonstrated. The performance of this photonic beamformer is experimentally demonstrated at 42.7 GHz in both transmission and reception modes. The progress achieved for realizing these architectures with integrated optics is also reported. Due to its advanced features (i.e., potential fast-switching, huge bandwidth, and immunity to electromagnetic interference), the architecture is a very promising alternative to traditional beamforming technologies for implementing beamformed base-station antennas in fixed and mobile broad-band wireless access networks operating in the millimeter-wave band. The study presented here has been carried out in the frame of the IST 2000-25390 OBANET project.**

***Index Terms*—Broad-band wireless access (BWA), microwave photonics, optical beamforming, phased-array antennas.**

I. Introduction

OPTICALLY beamformed phased-array antennas [1]–[8] have many advantages over their electrical counterparts such as small size, low weight, no susceptibility to electro-magnetic interference and wide instantaneous bandwidth and squint-free array steering (true-time delay). These two last features are very interesting for broad-band wireless access (BWA) networks, especially those operating in the millimeter-wave band, which are envisaged to fulfill the growing demand for bandwidth requirements of the recent and future multimedia services and applications. In the last decade, there has been an increasing interest on the research, trials and standardization of BWA networks due to features such as cost efficiency and deployment flexibility and scalability. A tremendous growth is expected for these networks in the next five years [9]. Several frequency bands (mainly at 28 and 40 GHz) have been allocated for these systems [10]. Also, a new generation of mobile broad-band systems (MBSs) operating in the millimeter wave will allow transference rates higher than 2 Mb/s, corresponding with the expected bandwidth demand in the coming years [11].

However, at high frequencies with high data rates, multipath fading and cross interference become serious problems which can be eased by using smart antenna technology (phased array with adaptive capabilities). Smart antennas have been traditionally controlled employing digital [12] or IF/RF processing [13] and can be employed to implement advanced services. Nevertheless, electrical beamforming networks have severe drawbacks when high-bit-rate signals at millimeter-wave bands are considered. These limitations can be overcome using optical beamforming techniques [1]–[8] in the base station, not only in transmission but also in reception mode.

In addition, very compact beamforming networks may be implemented using photonic integration techniques [14], [15], which alleviate the impact in system performance produced by the losses in optical and electrooptical interconnections. In this paper, the proposed beamformer is based in true time-delay (TTD) switching matrices. Optical TTD-switch matrices have the advantage of an almost unlimited RF bandwidth in combination with a potentially small device size, if the beamformer is integrated. Further the beamformer can be used in two directions, so that the same device can be used for forming the transmitter and the receiver beam.

This paper is structured as follows. Section II describes the proposed optical beamformer both in transmission and reception modes. In Section III, the development of photonic integrated circuits which comprise the photonic integrated beam-

Manuscript received June 21, 2005; revised October 15, 2005. This work was supported in part by the European Commission under Project OBANET IST-2000-25390 and Project GANDALF IST-1-507781 and by the Spanish Research and Technology Commission under Project TIC2000-1674.

M. A. Piqueras, B. Vidal, J. Herrera, J. M. Martínez, P. Sanchis, V. Polo, J. L. Corral, and J. Martí are with the Nanophotonics Technology Center, Universidad Politécnica de Valencia, 46022 Valencia, Spain (e-mail: jmarti@ntc.upv.es).

G. Grosskopf and M.-S. Choi are with the Fraunhofer-Institute for Telecommunications, Heinrich-Hertz Institute, 10587 Berlin, Germany.

A. Marceaux, J. Galière, J. Lopez, A. Enard, J.-L. Valard, O. Parillaud, E. Estèbe, and N. Vodjdani are with the Alcatel-Thales III–V Lab, 91460 Marcoussis, France.

J. H. den Besten, F. M. Soares, and M. K. Smit are with the COBRA Research Institute, Technische Universiteit Eindhoven, 5600 MB Eindhoven, The Netherlands.

Digital Object Identifier 10.1109/TMTT.2005.863049

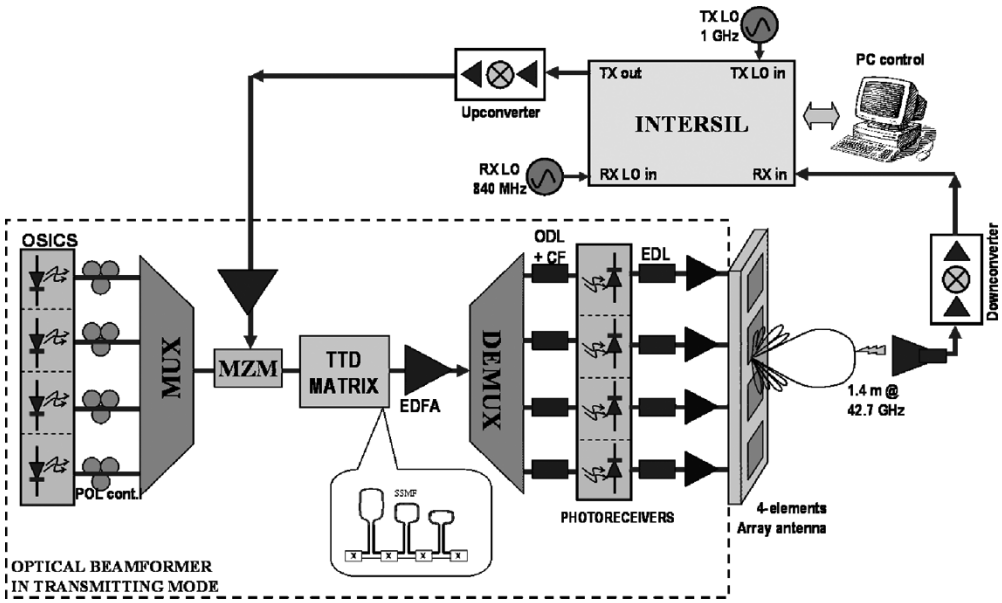

Fig. 1. Photonic beam-switched architecture for transmission mode.

former is reported. Recent advances in the packaging of 40-GHz photoreceivers are reported. In Section IV, experimental results for both modes are shown including radiation pattern measurements, broad-band data transmission/reception in the 40-GHz band and direction-of-arrival (DOA) estimation measurements. Finally, conclusions are provided in Section V.

This paper reports the work carried out in FP5 IST-2000-25 390 OBANET project.[1]

II. Beamforming Architecture Description

A. Transmission Mode

Fig. 1 shows a schematic of the transmitter part of the optical beamformer. The data is modulated by an RF-optical modulator onto four optical carriers at four equally spaced wavelengths, generated by a multiwavelength laser (MWL) source implemented by four independent laser sources. The four wavelengths are combined and externally modulated using an electrooptical Mach–Zehnder modulator (MZM). The modulating signal is generated by a commercial modulation/demodulation board, upconverted, and amplified using a millimeter-wave amplifier. Each wavelength is used to control the time delay for one of the four array antenna elements.

The MZM output is launched to the TTD switching matrix comprised by four cascaded optical switches. Standard single-mode fiber (SSMF) coils of lengths L, $2L$, and $4L$ are placed between the upper ports of consecutive switches. This optical TTD switch matrix is used to apply a controlled time delay that increases linearly with the wavelength of the optical carriers. The time delays for each wavelength can be controlled in eight steps, corresponding to eight different deflection angles. Therefore, the optical signal is routed through different aggregated lengths of fiber depending on the bias voltages of the switches, with up to eight different possible combinations (3 b). Due to the wavelength-dependent dispersive behavior of the optical fiber, each modulated optical carrier suffers a different time delay, depending on the selected path, given by

$$\tau = D \cdot L \cdot \Delta\lambda \tag{1}$$

where D is the dispersion parameter of the fiber, L is the length of the optical path, and $\Delta\lambda$ is the wavelength spacing between optical carriers. This relative time delay between optical carriers corresponds to different beam-steering angles according to

$$\theta_i = \arcsin(2 \cdot \tau_i \cdot f_{\mathrm{RF}}). \tag{2}$$

After the wavelenth-division multiplexing (WDM) optical signal is delayed and amplified using an erbium-doped fiber amplifier (EDFA), each optical carrier is demultiplexed and launched to a high-speed photodetector (PD). After amplification using an millimeter-wave amplifier, the four modulated electrical carriers are radiated using a $\lambda/2$ four-element patch antenna. The phase front of the radiated signal can be varied among eight different positions depending on the chosen combination of switching voltages (i.e., total delays), according to (2).

To avoid the carrier suppression effect, which can result in power degradation in the beamformer performance, single-sideband (SSB) modulation can be used [16]. In order to achieve SSB modulation, the optical carriers have been shifted 0.2 nm from the nominal central pass-band frequencies of the demultiplexer.

The length differences between each multiplexer/demultiplexer output and the antenna elements have to be compensated to avoid undesired time-delay differences among RF signals. In order to calibrate the relative time delays, one optical delay line (ODL) has been introduced before the PDs to allow fine time-delay adjustments. These ODLs can change its absolute time delay up to 300 ps, which is equivalent to 6 cm of SSMF with $n = 1.467$.

[1]OBANET. [Online]. Available: http://ist-obanet.upv.es

TABLE I
CORRESPONDENCE AMONG SWITCHING VOLTAGES, OVERALL DELAY, AND STEERING ANGLE WITH RESPECT TO BROADSIDE. (SWITCH CONTROL "0" CORRESPONDS TO CROSS STATE AND "1" TO BAR STATE)

Switching control	Total time delay (ps)	Steering angle (deg)
0110	0	-41.7683
1010	2.2440	-28.3257
0000	4.4880	-16.4301
1100	6.7320	-5.2331
0101	8.9760	5.7640
1001	11.2200	16.9818
0011	13.4640	28.9277
1111	15.7080	42.4808

To equalize the time delay from the demultiplexer to the antenna elements, first the absolute time delay (path length difference) between each branch (from the demultiplexer output to the PD) was determined employing an optical network analyzer, which can obtain fiber lengths with centimeter accuracy and using a mechanical measuring method for MZMs and PDs. After introducing patchcords to roughly compensate for these time delays, small time-delay errors of a few picoseconds caused by vector network analyzer noise and accuracy as well as differences between consecutive connections of the electrical cables remain. Since the time delay needed for beam-steering is of the order of picoseconds, these errors have to be compensated for.

Therefore, a complementary procedure to obtain fine time-delay calibration was employed, based on measuring the radiation pattern of pairs of antenna elements and, by means of the angle position of the radiation nulls, derive the time delay between them. Although this fine calibration is based on phase adjusting, thanks to the previous coarse calibration, time delay can be calibrated without ambiguity. Finally, in order to steer the beams to positive and negative angles relative to the center of the sector (broadside), a fixed time shift of (15.7/2) ps to each adjacent element were included. Thus, positive and negative steering angles can be obtained as can be seen in Table I.

B. Reception Mode

The schematic of the 3-bit beamformer in the reception mode is shown in Fig. 2. The 155-Mb/s 32-QAM modulating signal at 1 GHz was generated using a broad-band modem arbitrary board. This IF signal was upconverted to the millimeter-wave frequency band before being radiated. The received signal at the array antenna elements is translated to the optical domain using as many electrooptical MZMs as antenna elements, i.e., four MZMs for a four-element antenna. Each amplitude modulated optical carrier is proportionally delayed by the TTD unit. Finally, the four optical modulated carriers are photodetected using a single photodiode, and the detected signal is downconverted to IF and demodulated.

The same time-delay calibration procedure that was described for the transmitting mode was used in the reception scheme. In this case, the ODLs are placed after the MZMs. The absolute time delay (path length difference) between each branch (from the MZM to the multiplexer output) was again determined employing an optical network analyzer, and fine calibration was carried out by derivation of the time delay between adjacent antenna elements from measurements of the angular position of the radiation nulls.

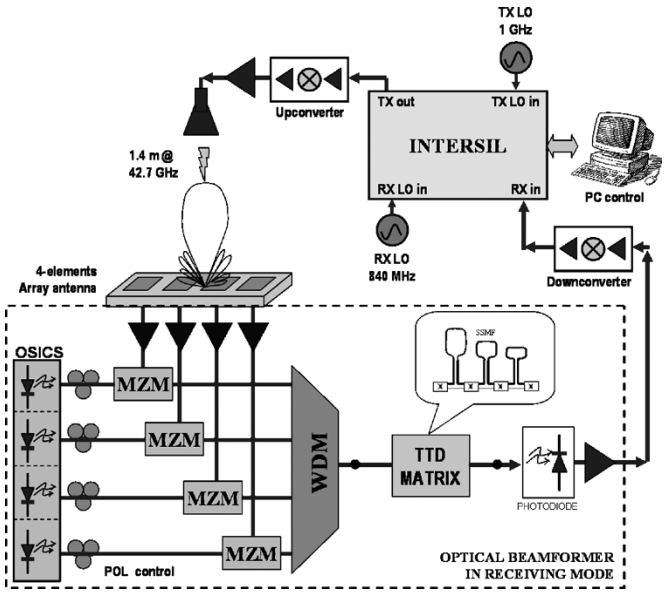

Fig. 2. Photonic beam-switched architecture for the reception mode.

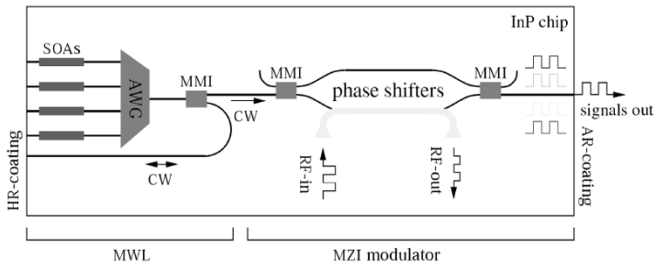

Fig. 3. Schematic of the transmitter driver chip.

III. PHOTONIC INTEGRATED BEAMFORMER

The beamformer, as described in Section II-A, consists of several optical, microwave, and opto-electronic components. To reduce connection losses and reduce system complexity, integration is highly desirable.

As an example, the optical source with modulator is considered. If the beamformer would be assembled using standard components, one would need four wavelength-tunable lasers, a four-to-one coupler, and a high-speed intensity modulator. The use of an MWL integrated with a Mach–Zehnder interferometer (MZI) modulator (Fig. 3) has the same functionality as the above-mentioned six components. This reduces the number of fiber-chip couplings from five to one. For an integrated receiver driver chip, an even greater integration level is achieved. Next, the integrated TTD switch implementation is described. Finally, the fabricated photoreceiver modules which are part of the receiving side of the beamformer described in Section II-A are reported, and future technological improvements for low-cost collective wiring of photoreceiver modules are outlined.

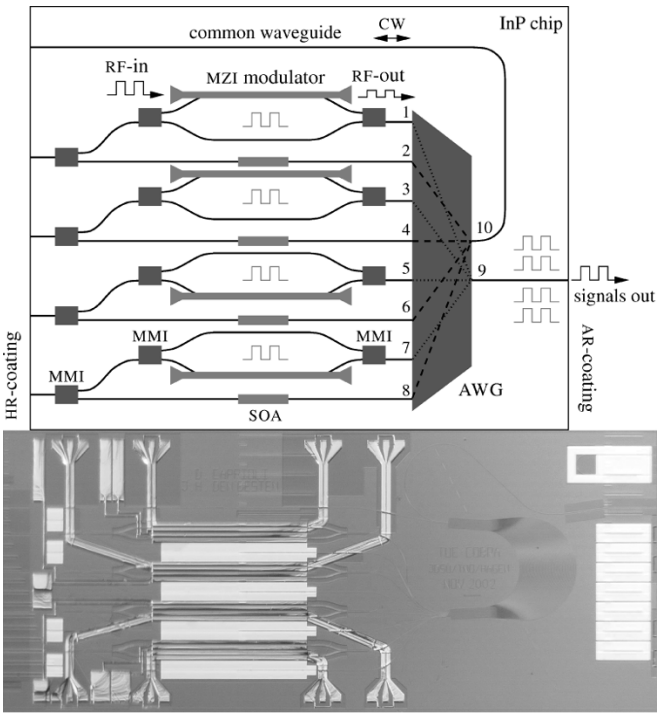

Fig. 4. Schematic and photograph of an integrated receiver driver chip.

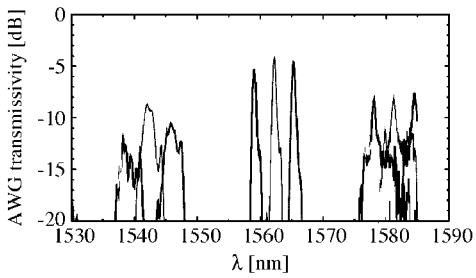

Fig. 5. Measured chirped AWG passbands.

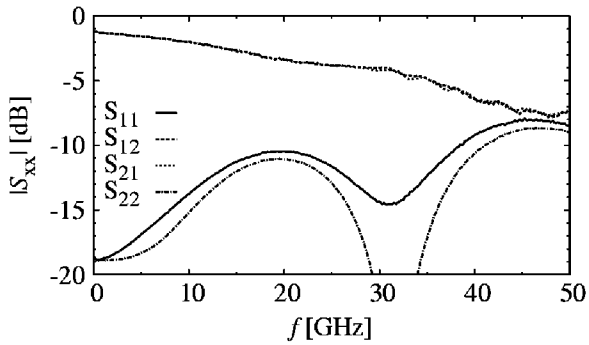

Fig. 6. Measured small-signal S-parameters of a modulator with a phase-shifter length of 2 mm.

A. MWLs on InP

The transmitter driver chip is an MWL integrated with an MZM, of which a schematic is shown in Fig. 3. The MWL consists of an array of semiconductor optical amplifiers (SOAs) in combination with an arrayed waveguide grating (AWG) that acts as an intracavity filter [17]. Laser action takes place in the Fabry–Perot cavity that is created by reflections between the multiplexed output facet and the respective facets at each SOA. Power is coupled out of the cavity using a multimode-interference (MMI) coupler. The CW-output power of each laser is typically about 1 mW [18].

Each laser in the transmitter driver chip can be controlled over a range of 5 dB by adjusting the bias current through the amplifier. Since each wavelength corresponds to a particular antenna element, the beam shape can be adapted by changing the amplifier current. Radiation pattern nulls can be slightly moved by changing array amplitude distribution.

The circuit scheme of an integrated receiver driver chip is shown in Fig. 4. In the receiver driver, which is different from the transmitter driver, four modulators are required because the signals coming from the four receiver antenna elements are different. Our device has a novel circuit architecture consisting of a four-channel MWL with four RF MZI modulators. A conventional approach would need three (de)multiplexers: one in the MWL and two at both ends of the four modulators, for demultiplexing and multiplexing the four wavelengths before and after modulation, respectively. This introduces complications: a large chip space is needed, and all multiplexers should be accurately tuned to each other. A much more compact circuit design would be possible with the modulator integrated in the laser cavity. This is not possible, however, because a modulator inside the cavity would make the laser unstable and too slow for gigahertz operation because of the large cavity length. Fig. 4 shows a schematic and a chip photograph of a new approach that performs all required multiplexing and demultiplexing operations with a single AWG. By using just one AWG, the device size is small, and possible AWG misalignment problems are avoided. The AWG has two inputs and eight outputs.

To explain the operating principle of this laser, we refer to Fig. 4 in which all AWG ports are labeled. At the right side of the AWG, the port with label 9 is the common output for fiber coupling and the port with label 10 is the common output that leads to a high-reflection (HR)-coated facet. This waveguide is part of the laser cavity. At the left side of the AWG, the demultiplexed ports are labeled 1 to 8. The even port numbers (i.e., 2, 4, 6, and 8) are each part of a different laser cavity (one for each wavelength) and are connected to eight optical amplifiers. From there, the cavities are completed by waveguides that lead to the HR-coated facet. In each cavity, a 1×2 MMI is included to couple half of the light reflected from the facet out of the cavity. This light is routed to a separate MZM. The modulators each modulate the microwave signals onto the optical carrier coming from the laser cavities.

Since an AWG is an imaging device, light applied to an adjacent input port will be imaged onto an adjacent output port. Consequently, the four modulated signals at the odd port numbers (i.e., 1, 3, 5, and 7) are multiplexed by the AWG into output port 9.

The AWG has been chirped to suppress lasing operation in unwanted orders of the AWG. The recorded spectrum in Fig. 5 shows that adjacent orders are sufficiently suppressed by the AWG to prevent lasing at these wavelengths.

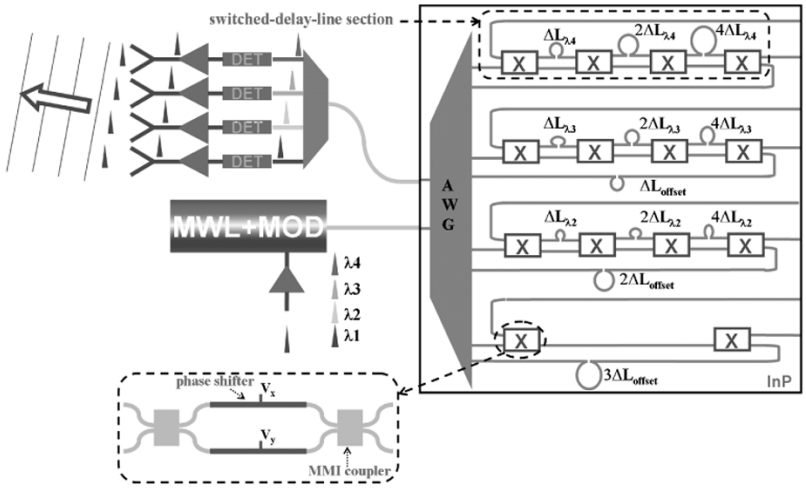

Fig. 7. Schematic diagram of the proposed beamforming circuit showing the implementation of the TTD photonic integrated beamformer.

B. 40-GHz MZM on InP

One of the most important specification for high frequency modulators, after bandwidth, is a high efficiency which is obtained by a long interaction length. This means that the optical and RF wave need to have identical velocities and that the RF wave has low attenuation.

InP technology has the clear advantage, over for instance $LiNbO_3$, that integration with active components like lasers, SOAs and detectors is possible. By using p-i-n diode structures on InP, one is able to concentrate the electrical field in the region where it can interact with the optical wave, thus forming an efficient modulator. Typically, such a structure is bandwidth-limited by its large velocity and impedance mismatch as well as high microwave attenuation down to 10 Gb/s [19], [20].

One solution to these bandwidth limitations is to implement a capacitively loaded structure [21]. Its periodical phase-shifter loading combines a velocity and impedance match with a low absorption, but reduces the electrooptical efficiency and, consequently, increases the device length. We have chosen a solution that is easier to implement and does not sacrifice efficiency: by reducing the phase-shifter waveguide width down to 1 μm, we can combine good modulation efficiency with velocity and impedance matching [22]. Measured small-signal S-parameters shown in Fig. 6 show a 6.4-dBc bandwidth of $\sim$40 GHz. Characteristic impedance and V_π were measured to be 55 Ω and 6 V, respectively. We are working on integrating the modulators and lasers on a single chip. Fig. 4 shows a photograph of a first version of the integrated device, which revealed some problems that are presently being resolved.

C. Digital TTD Switch on InP

Fig. 8 shows a schematic layout of the fabricated integrated TTD beamformer. The four optical wavelengths, which have been simultaneously modulated with the 40-GHz signal to be transmitted, are first demultiplexed onto four different waveguides by the AWG. Then, each wavelength is coupled to a 3-bit switched-delay-line (SDL) section, which consists of four cascaded 2×2 electrooptic MZI switches. A major advantage of these switches over thermal SiO_2 switches is their switching time, which is in the order of a few nanoseconds. The 2×2 switches in each SDL section (except for the reference wavelength) are cascaded by a bypass line on one of the outputs and by a delay line (with a length ratio of 1 : 2 : 4 for the first, second, and third delay lines) on the other. By applying a bias voltage to one of the branches of the MZI switches (see the inset of Fig. 7), each wavelength can be selected to go through or to bypass one or more of the three delay lines. In this way, the optical path lengths of each individual wavelength can be set individually. Accurate time delays can be achieved through submicrometer-level control of the lengths of the waveguide-based delay lines. The delay-line lengths have been dimensioned in such a way that the path-length differences between the adjacent wavelengths are linearly progressive for all eight possible settings of the beamformer. The longest delay line (which has a propagation delay of 34 ps) is 2831-μm long, and the shortest delay line (3 ps) is 236 μm. The waveguides going from the SDL sections back to the AWG have lengths that are linearly increasing with the wavelength (which is symbolized by the offset delay lines ΔL_{offset} in Fig. 7), in order to be able to introduce positive as well as negative progressive time delays. Finally, the four wavelengths are multiplexed by the AWG and coupled out of the chip. A photograph of the fabricated beamformer is shown in Fig. 8. It is very compact: chip dimensions of this fully integrated device are 8×10 mm^2.

Two types of optical waveguides were used to realize the beamformer: shallowly etched waveguides for low-loss propagation and deeply etched waveguides with a very short bending radius for reducing the dimensions of the circuit. The beamformer showed an on-chip optical power loss of around 27 dB for $\lambda 2, \lambda 3$, and $\lambda 4$ and 21 dB for the reference wavelength $\lambda 1$ (see Fig. 9). After measurements on test structures, the on-chip losses were attributed to the following components in the optical path of each wavelength: 2×4.0 dB for the AWG (dimensions $= 1.3 \times 1.3$ mm^2), 4×2.4 dB for the MZI switches, 4.2 cm $\times$ 0.7 dB/cm for the shallowly etched waveguide propagation losses, 0.5 cm $\times$ 1.9 dB/cm for the deeply etched waveguide propagation losses, 22×0.2 dB

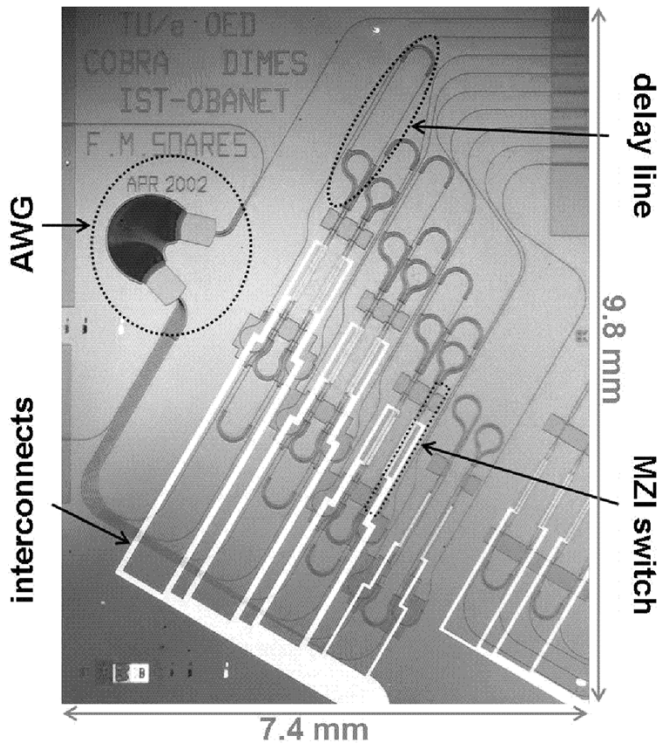

Fig. 8. Fabricated integrated beamformer chip.

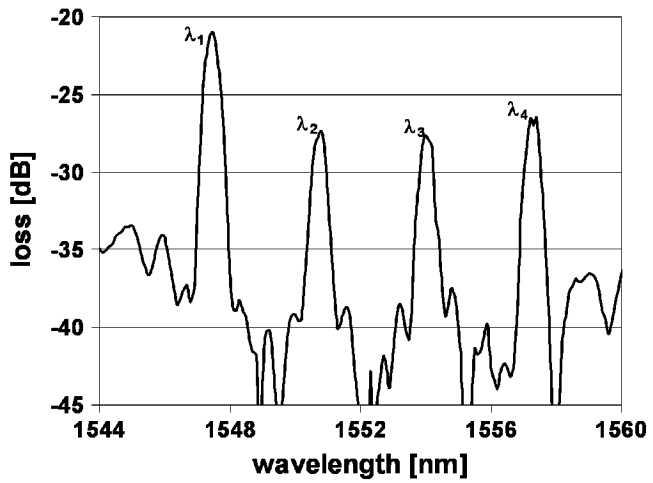

Fig. 9. Plot of the optical spectrum through the fabricated beamformer. The first wavelength $\lambda 1$ shows lower losses because it is the reference wavelength that does not go through any SDL section.

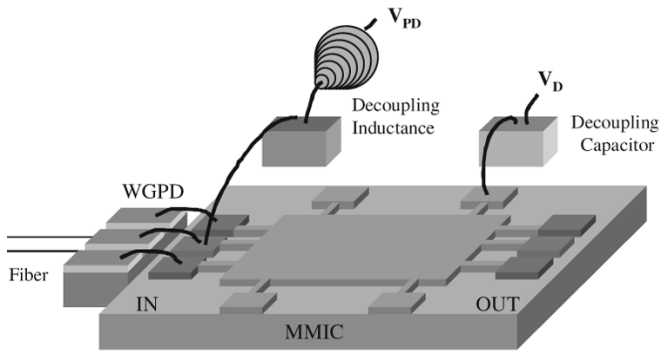

Fig. 10. Schematic representation of a hybrid photoreceiver.

for the transitions from shallow to deep waveguides, and $1080^\circ \times 0.2$ dB/360° for the deep-waveguide bending losses. The operating wavelengths of the device ranged from 1537 to 1557 nm in discrete steps of 3.2 nm. The device showed a shift of 0.4 nm in wavelength between TE- and TM-polarized input, which is not a problem for beamformer applications because the input signal is TE-polarized. The switching voltages of the reversely biased p-i-n-diode phase shifters of the MZI switches were around -6 V, and the switching speed, measured from the bond pad, was smaller than 5 ns. This switching speed can be further reduced by minimizing the metal-interconnect lengths from the bond pads to the electrooptic phase shifters. The scan speed for the whole coverage area of the beamformer is eight time the switching time ($<$ 40 ns). DOA estimation is possible by configuring the TTD switch to sweep through all eight possible directions and measuring the received power for each direction. The direction with the highest power indicates the DOA.

The functionality of the device as a TTD beamfomer was confirmed by time-delay measurements with a vector network analyzer (VNA). The RF output signal from the VNA was modulated onto an optical carrier and then coupled to an SDL section. At the output of the beamformer, the RF signal was detected by a PD and fed back into the VNA. By sweeping the output RF frequency from dc to 10 GHz, the VNA monitors the phase of the input RF signal with respect to the RF output signal for the different frequencies, from which the propagation delay can be extracted. Time-delay measurements of several delay lines were performed, which showed a relative accuracy of 5% with respect to the design values [23].

In the next redesign, the TTD circuit will be integrated with spot-size converters, with which the coupling loss from the InP waveguide to a SSMF (and vice versa) can be reduced from 10 to 1.5 dB [24].

D. 40-GHz Photoreceiver Modules

Being part of the receiving side of the beamformer described in Section II-A, hybrid 40-GHz photoreceiver modules have been fabricated. As shown in Fig. 10, it comprises a 40-GHz waveguide photodiode (WGPD) and a narrow-band monolithic-microwave integrated-circuit (MMIC) amplifier. The WGPD is fed by an input-lensed optical fiber, and the amplifier is connected to an output RF connector.

The frequency response of the photoreceiver module, which was measured under an optical power of 0 dBm, is shown in Fig. 11. We observe that, in the 40.5–43.5-GHz frequency band, the RF power has a mean value of -3 dBm with a flatness of ± 0.5 dBm (which is equal to the gain flatness of the MMIC alone). For a similar input optical power, an output RF power of -24 dBm was measured on the WGPD chip at 40 GHz. Considering the nearly 20 dB of gain of the MMIC at 40 GHz, this leads to an RF output power for the module of -4 dBm at 40 GHz, which is in agreement with the measurement. This indicates that

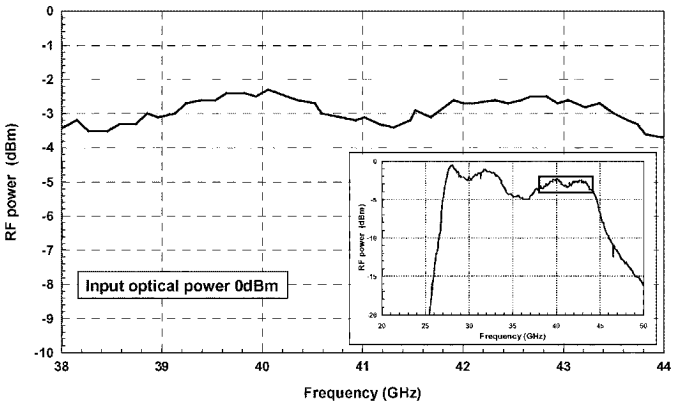

Fig. 11. Frequency response of the 40-GHz hybrid module.

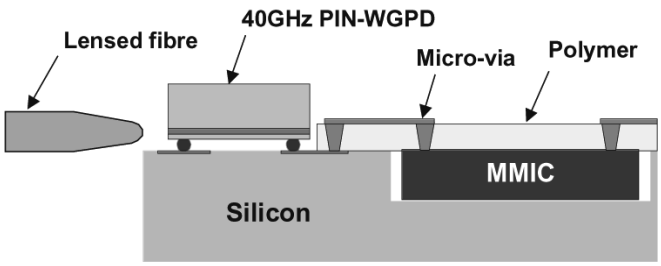

Fig. 12. Schematic representation of the compact photoreceiver.

the packaging does not lead to any additional losses or degradation compared to the WGPD and MMIC frequency response alone.

A new approach is proposed to improve the fabrication yield as well as the dispersion of the performances of 40-GHz photoreceiver modules. It is based first on the microwave high-density interconnection (MHDI) technology and, second, on 40-GHz WGPD with relaxed coupling tolerances.

The MHDI technology has been shown to be effective for the packaging of high-frequency MMIC active devices up to 60 GHz [25]. Compared to wire bonding, the main advantages of this concept are a better reproducibility of interconnect and a lower cost thanks to collective processing. Except for component gluing, all of the technological steps are realized in a collective way for several modules. As shown in Fig. 12, it is based on the integration of the MMIC die and passive components (e.g., decoupling capacitors and filters) onto an Si substrate. The process includes silicon metallization and micromachining (reactive ion etching), photo-etching, component gluing, polymer (Arlon) gluing, and metallization, via hole opening (laser ablation).

In order to evaluate the impact of the MHDI technology on the performances of the amplifier alone at 40 GHz (without the PD), a test vehicle including the same MMIC amplifier than used in hybrid modules has been designed and realized. It comprises input and output RF pads for measurements. In Fig. 13, the measured S-parameters are compared with the datasheet values given for the bare die. Correct matching and gain responses have been achieved except for a frequency shift (around 2.5 GHz) of the 40-GHz MMIC in the MHDI structure. This

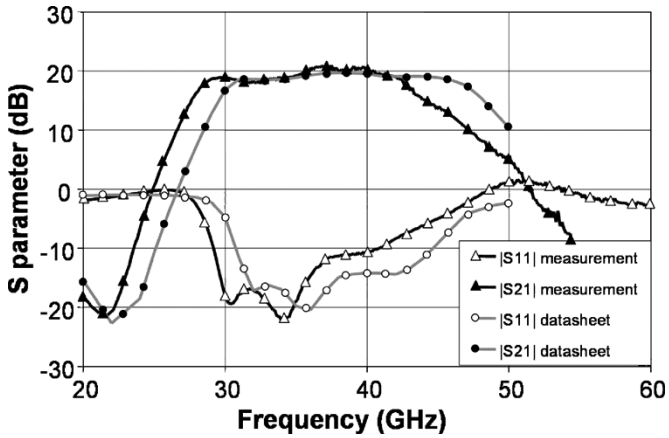

Fig. 13. Measurement of S-parameters (S_{21} and S_{11}): comparison between the bare die and the active test vehicle.

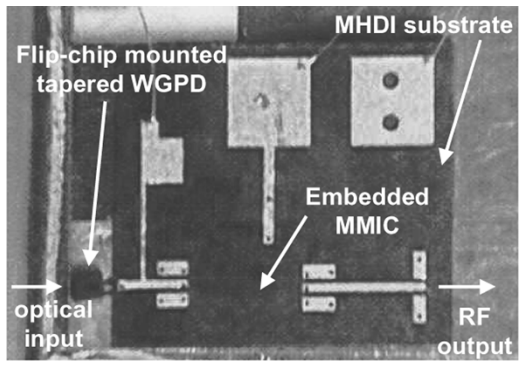

Fig. 14. Photograph of the compact photoreceiver.

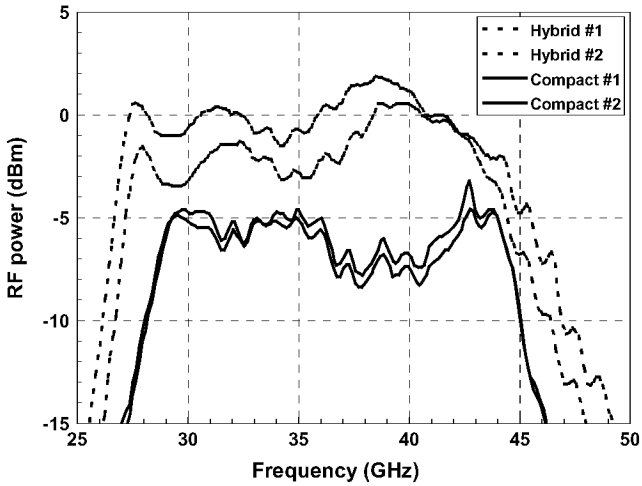

Fig. 15. Frequency response of the compact photoreceiver.

shift can be explained by the passivation of MMICs with benzocyclobutene (BCB) before MHDI process. However, MMIC suppliers foresee more and more the passivation of MMICs with optimized design taking into account this passivation. This result confirms the ability of the MHDI technology to interconnect high-frequency MMIC devices.

The positioning tolerances of a standard 40-GHz WGPD toward optical lensed fiber are typically ± 1.6 and ± 0.7 μm in lateral and vertical directions, respectively. These values are

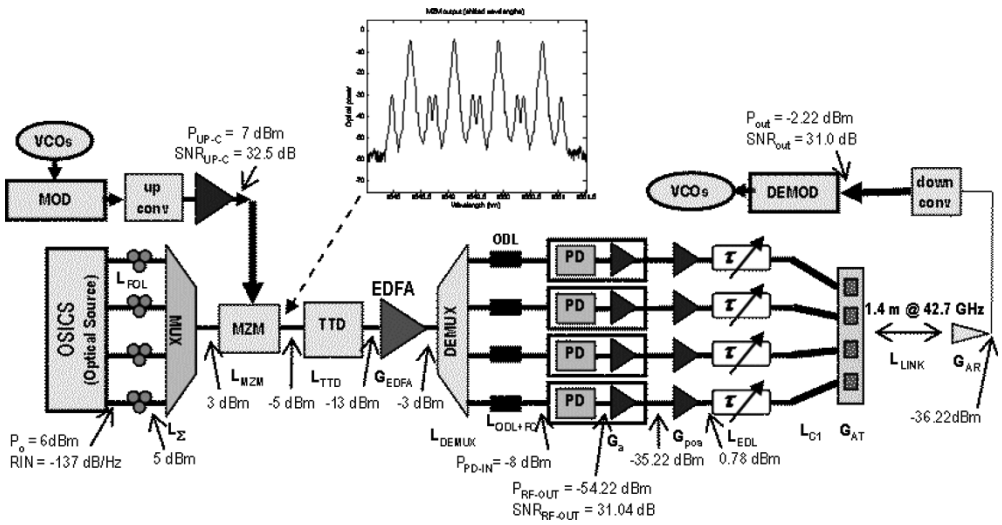

Fig. 16. Transmission-mode experimental setup.

not compatible with passive coupling by using a standard pick and place machine, which is an ultimate goal for the fabrication of low-cost optoelectronic modules. To improve this feature, WGPD with high alignment tolerances toward optical fiber have been developed, thanks to the integration of a passive tapered input waveguide with large coupling tolerances. The optical power is transferred to the absorbing waveguide by vertical evanescent coupling [26]. Lateral and vertical -1-dB coupling tolerances with a lensed fiber as high as ± 2.6 and $-1.7/+1$ μm, respectively, have been measured on devices based on this principle. This result is very good when compared to the coupling tolerances observed on standard WGPDs, since it corresponds to an improvement of 70% and 90% in the lateral and vertical directions, respectively. The PD used in this study, based on this technology, exhibits a responsivity of 0.35 A/W with a lensed fiber (without antireflection (AR) coating) and a cutoff frequency of 30 GHz.

Two compact photoreceiver test vehicles have been realized. Tapered WGPD equipped with gold stud bumps have been flip-chip mounted on the MHDI substrate by the thermo compression process. Fig. 14 shows a photograph of the resulting compact photoreceiver. The area for the mounting of the photodiode is composed of gold pads with a pitch that is identical to the coplanar access one of the PDs. The biasing of the PD is realized through a stub which can be considered as an open circuit in the frequency range of interest.

The frequency response has been measured by a heterodyne technique, as shown on Fig. 15. The result is compared to the frequency response of two hybrid photoreceiver test vehicles (without package) measured under the same conditions. To facilitate the comparison, all of the curves are normalized to 1-mA dc current flowing in the PD. One can notice that the dispersion of the performances of the compact test vehicles is lower than that for the hybrid test vehicles, thus showing the better reproducibility of this technology. The general behavior of the compact test vehicles is comparable to hybrid test vehicles. According to the measurement made previously on the MMIC alone, the 2.5-GHz shift of the frequency response is

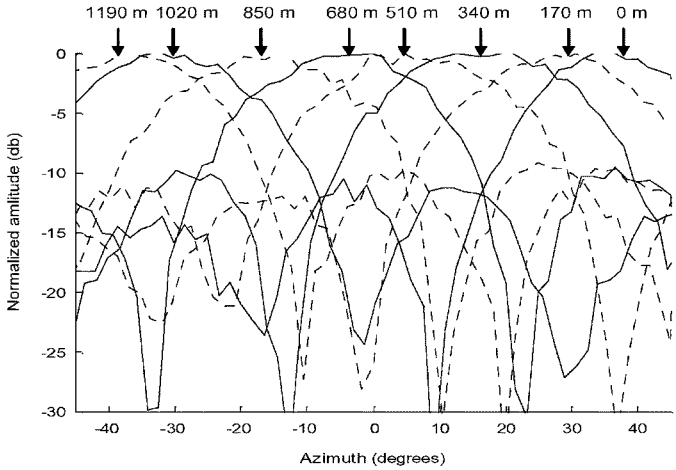

Fig. 17. Measured radiation pattern at 40 GHz for the eight-beam positions in transmission mode.

also observed. However, the absolute RF output power remains inferior by approximately 5–7 dB. It should be noticed that the bandwidth of the tapered WGPD is lower than that of the standard WGPD used in the hybrid test vehicles, leading to additional RF losses at 40 GHz of roughly 2 dB. The remaining losses are therefore in the 3–5-dB range. We can attribute these losses to two factors, which are: 1) the flip-chip mounting of the photodiode give rise to RF losses because of a mismatch between the characteristic impedances of the photodiode and the gold pads [27] and 2) the distance between the PD and the MMIC is too important, leading to resonance in the frequency range of interest. Further experiments are thus necessary to fully control this new packaging technology. In particular, the impact of the flip-chip mounting on the frequency response needs to be investigated.

IV. Experimental Results

A. Transmission-Mode Performance Evaluation

The setup used to measure the performance of the beamforming network in the transmission mode is depicted in Fig. 16,

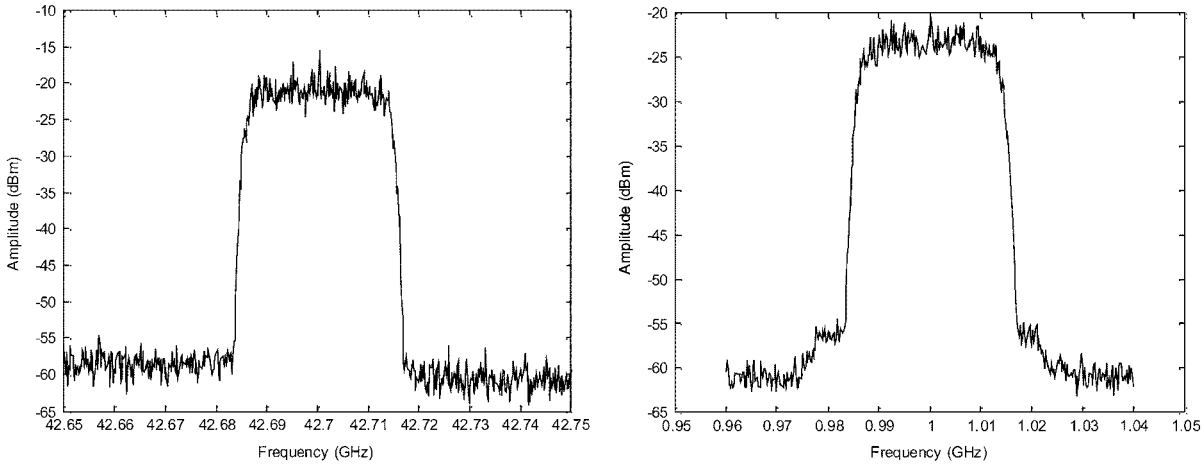

Fig. 18. Electrical spectrum of the transmitted signal: (a) at the MZM input and (b) at the demodulation board input, after detection and downconversion to 1 GHz.

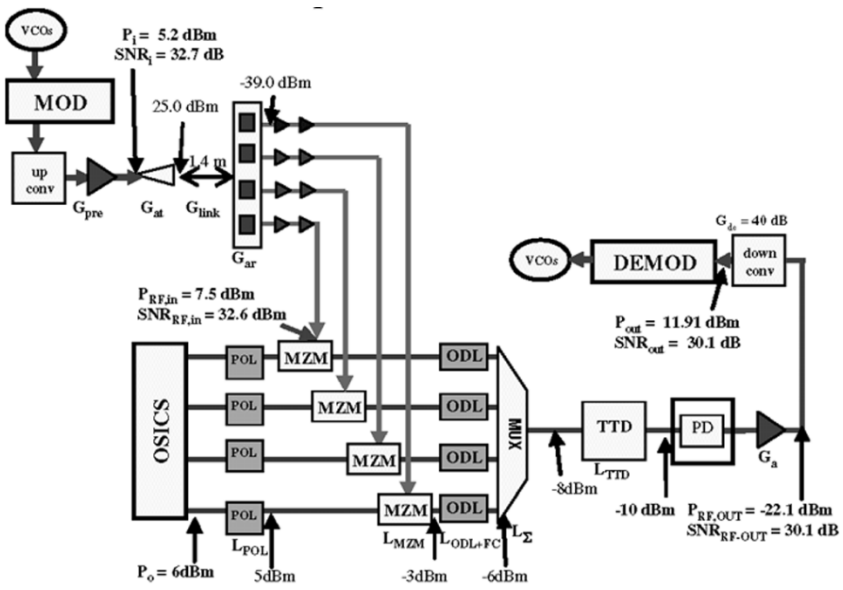

Fig. 19. Reception-mode experimental setup.

where the power budget and the four modulated optical carriers' spectra at the MZM output are also shown.

The 155-Mb/s 32-QAM modulating signal at 1 GHz was generated using a commercial modulation/demodulation arbitrary board. After filtering, the signal was electrically upconverted to 42.7 GHz, and the modulated RF carrier power was amplified up to +7 dBm, where its signal-to-noise ratio (SNR) was 32.5 dB. This signal was impinged into the MZM. The modulated WDM signal was launched to the 3-bit TTD switching matrix, which was controlled by a four-output external tunable bias source. The lengths of the SSMF fiber coils used to implement the time delays were 170, 340, and 680 m, corresponding to a binary delay line. An ODL placed before each photoreceiver was used for calibration purposes, as explained in Section II. The detected RF signal is further amplified using a 36-dB-gain millimeter-wave amplifier and radiated using the four-element patch antenna. After propagation through a 1.4-m radio link (far field at 42.7 GHz), a 40-dB-gain electrical downconverter, fed

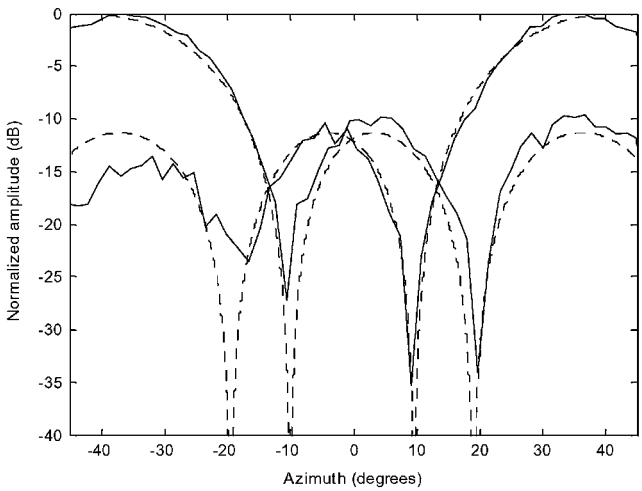

Fig. 20. Measured antenna radiation pattern over the 90° sector in the receiving mode.

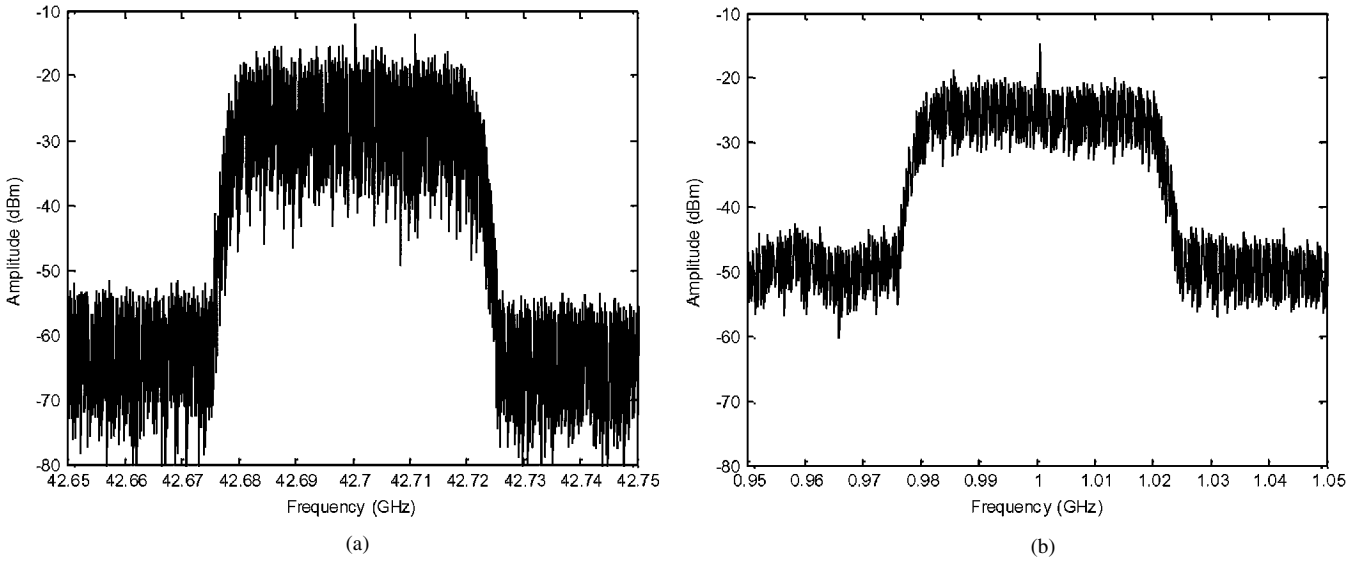

Fig. 21. Electrical spectrum of the 42.7-GHz transmitted signal: (a) at the antenna input and (b) at the demodulation board output, after detection and downconversion to 1 GHz.

by a 40-GHz horn antenna, downconverts the 42.7-GHz signal back to 1 GHz. The measured output SNR was 31 dB for a −2.22-dBm signal power at 1 GHz. The IF signal was demodulated by a second modem board, which allows us to measure signal quality parameters such as the bit error rate (BER). The measurement setup consisted of a computer-controlled platform suited to obtain radiation pattern diagrams. The downconverter was mounted in a post that could be moved along a 90° circumference arch using a computer-controlled step engine, with programmable speed, acceleration, and angular step size.

Fig. 17 shows the measured radiation patterns corresponding to the delay and steering angles shown in Table I. The experimental results agree quite well with theory, which are not shown for the sake of clarity. The measured −3-dB beamwidth also agrees very well with theory [28].

The feasibility of the proposed optically beamformed antenna in transmission mode was confirmed by radio transmission experiments in the 40-GHz band. A 32-QAM 155-Mb/s 1-GHz signal was generated, beamformed, and radiated employing the experimental setup described previously.

Fig. 18 shows the measured 155-Mb/s 32-QAM signal spectra at the MZM input and at the demodulation board input. Error-free operation was achieved using 255/256 Reed–Solomon forward error correction (FEC) codes.

The experimental setup SNR was limited due to the 1-dB interception point of the upconverter, which imposed +7-dBm output power level for distortion-free operation. The SNR can be improved using a higher linearity upconverter; nevertheless, the optical beamformer is almost transparent, introducing a SNR degradation of 1.5 dB.

B. Reception Mode Performance Evaluation

The experimental setup of the 3-bit beamformer in reception mode is shown in Fig. 19, which is similar to the transmission-mode setup.

The 155-Mb/s 32-QAM modulating signal at 1 GHz was generated using a modem arbitrary board. This IF signal is upconverted to the millimeter-wave frequency band before being radiated. The received signal at the antenna elements is translated to the optical domain using four MZM corresponding, with an element-to-element correspondence. The lengths of the SSMF fiber coils are the same as those used in the transmission experiment (i.e., 170, 340, and 680 m). Finally, the four optical modulated carriers are photodetected using a single PD. The detected signal is downconverted to IF and demodulated.

The beam patterns for two of the eight beam-steering angles have been measured. In Fig. 20, these measurements are depicted and compared with the theoretical prediction. An excellent match between both the theoretical and measured results can be seen.

Several modulation formats (QPSK, 8 PSK, 16 QAM, and 32 QAM) have been evaluated to demonstrate the beamforming capability for high-data-rate transmissions. Error-free operation was obtained for all modulation formats except for 32-QAM, for which a BER of 10^{-6} was obtained using Reed–Solomon and 4/5 convolutional codes when a payload rate of 155 Mb/s was transmitted. Fig. 21 shows the measured electrical spectra at the input and output of the beamformer, including radio transmission of the 32-QAM modulated carrier at 42.7 GHz.

The detected-signal SNR measured by the demodulation board was 25 dB and was limited due to the 1-dB interception point of the upconverter, which imposed a low-output-power limit for distortion-free operation. From the measured output SNR, it can be derived that the optical beamformer introduces an SNR reduction of around 4 dB. Since the SNR is mainly limited by the electrical subsystem, it can be improved using an upconverter with higher linearity. The received constellation of the 155-Mb/s 32-QAM signal is depicted in Fig. 22 for both the transmission and reception modes.

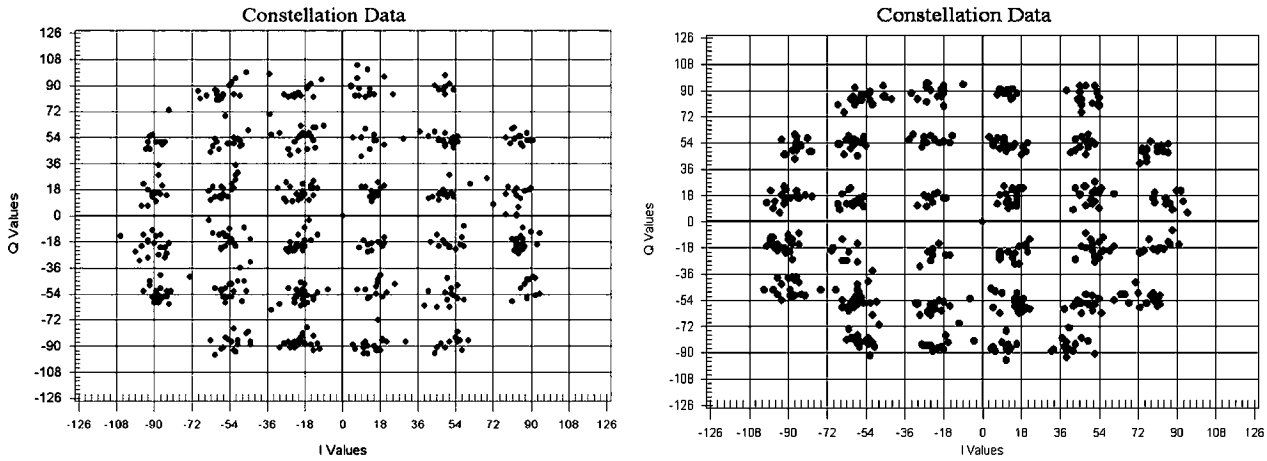

(a) (b)

Fig. 22. Received constellation of the 155-Mb/s 32-QAM signal: (a) after detection in transmission and (b) in reception mode.

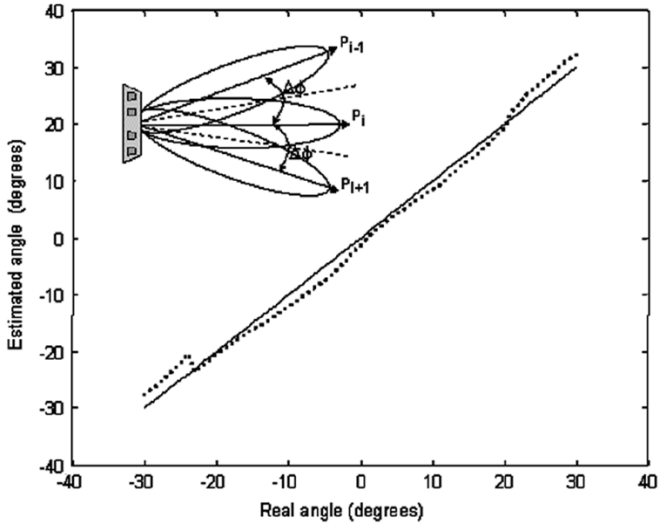

Fig. 23. Estimated angle as a function of the real angle of the terminal. The dotted line corresponds to the experimental results while the solid line depicts the ideal performance. The inset shows the schematic of the proposed DOA algorithm.

C. DOA Estimation

The DOA estimation is a key functionality in both the fixed and mobile scenarios to implement user-tracking and location-based services. Conventional digital-signal-processing (DSP)-based DOA estimation algorithms, such as MUSIC or ESPRIT, have been proven to achieve good results. However, they require increased processing power and are difficult to implement in real-time systems, especially when high data bit rates are considered. Therefore, DOA estimation has been proposed [29], [30] by means of a heuristic approach based on signal power measurements of three adjacent beams using an estimator given by

$$d = \frac{P_{i+1} - P_{i-1}}{P_i} \tag{3}$$

where P_i is the measured power at each beam direction as depicted in Fig. 23. The experimental demonstration of DOA estimation has been carried out by using the previously described optically beamformed beam-switched antenna. Fig. 23 shows the estimated angle as a function of the real angle of the terminal. The dotted line corresponds to the experimental results, while the solid line depicts the ideal performance. It can be seen that a good accuracy of the estimation is achieved. A maximum DOA estimation error of 3.66° with an rms error of 0.77° was obtained.

V. Conclusion

A 3-bit photonic beamforming network based on 2×2 optical switches and dispersive media has been proposed and its performance experimentally validated for broad-band data transmission in the 40-GHz band. Error-free 42-GHz transmission of M-QAM 155-Mb/s data has been achieved in both the transmission and reception modes. In both cases, the optical beamformer is almost transparent, thus introducing a small SNR degradation. The radiation patterns in both transmission and reception modes have been measured, showing a good agreement with theory. DOA estimation has been also experimentally evaluated, showing a good agreement between measurements and theory.

Also, the progress in the photonic integration of different beamformer subsystems has been reported. Recent advances in the packaging of 40-GHz photoreceivers have been reported. In particular, a compact photoreceiver has been fabricated based on two innovative technologies. First, the MHDI technology has been shown to be effective for the packaging of high-frequency MMIC active devices. This leads to a better reproducibility of interconnect and a lower cost thanks to collective processing. Second, 40-GHz WGPDs with high coupling tolerances have been developed that are compatible with flip-chip mounting and passive optical coupling.

Acknowledgment

The authors would like to thank Project Officer Dr. F. Medeiros, OBANET, for his continuous support and fruitful recommendations.

REFERENCES

[1] W. Ng, A. Walston, G. Tangonan, J. Newberg, J. J. Lee, and N. Bernstein, "The first demonstration of an optically steered microwave phased array antenna using true-time delay," *J. Lightw. Technol.*, vol. 9, no. 9, pp. 1124–1131, Sep. 1991.

[2] R. D. Esman, M. Y. Frankel, J. L. Dexter, L. Goldberg, and M. G. Parent, "Fiber optic prism true time delay antenna feed," *IEEE Photon. Technol. Lett.*, vol. 5, no. 11, pp. 1347–1349, Nov. 1993.

[3] D. T. K. Tong and M. C. Wu, "A novel multiwavelength optically controlled phased array antenna with a programmable dispersion matrix," *IEEE Photon. Technol. Lett.*, vol. 8, no. 6, pp. 812–814, Jun. 1996.

[4] J. L. Corral, J. Martí, S. Regidor, J. M. Fuster, R. Laming, and M. J. Cole, "Continuously variable true time-delay optical feeder for phased-array antenna employing chirped fiber grating," *IEEE Trans. Microw. Theory Tech.*, vol. 45, no. 8, pp. 1531–1536, Aug. 1997.

[5] H. Zmuda and E. N. Touglian, *Photonic Aspects of Modern Radar*. Norwood, MA: Artech House, 1994.

[6] B. Vidal, J. L. Corral, M. A. Piqueras, and J. Martí, "Optical delay line based on arrayed waveguide gratings' spectral periodicity and dispersive media for antenna beamforming applications," *IEEE J. Sel. Topics Quantum Electron.*, vol. 8, no. 6, pp. 1202–1210, Nov./Dec. 2002.

[7] M. A. Piqueras, B. Vidal, J. Herrera, V. Polo, J. L. Corral, and J. Martí, "Optical switched beamformer for broad-band wireless access networks at 40 GHz in receiving mode," presented at the 30th Eur. Conf. Opt. Commun. (ECOC), Stockholm, Sweden, Sep. 5–9, 2004.

[8] B. Vidal, M. A. Piqueras, J. Herrera, V. Polo, J. L. Corral, and J. Martí, "Experimental demonstration of a 3-bit photonic beamformer at the mm-band in transmission and reception modes," presented at the Int. Microw. Photon. Top. Meeting.

[9] M. Peruyero, "The current status of broad-band wireless access and ideas on future development," presented at the Broad-Band Fixed Wireless Access Workshop, Brussels, Belgium, Mar. 2001.

[10] *IEEE Standard for Local and Metropolitan Area Networks. Part 16: Standard Air Interface for Fixed Broad-Band Wireless Access Systems*, 2001.

[11] "Report on MBS applications and services,", The MBS Project, CEC Deliverable MBS/CT1/T1.2/BBC016.1, 1996.

[12] S. Rappaport, *Smart Antennas, Adaptive Arrays, Algorithms & Wireless Position Location*. Piscataway, NJ: IEEE Press, 1998.

[13] *Phased Array Antenna Handbook*, R. J. Mailloux, Ed., Artech House, Norwood, MA, 1994.

[14] R. Nagarajan, C. H. Joyner, R. P. Schneider, Jr., J. S. Bostak, T. Butrie, A. G. Dentai, V. G. Dominic, P. W. Evans, M. Kato, M. Kauffman, D. J. H. Lambert, S. K. Mathis, A. Mathur, R. H. Miles, M. L. Mitchell, M. J. Missey, S. Murthy, A. C. Nilsson, F. H. Peters, S. C. Pennypacker, J. L. Pleumeekers, R. A. Salvatore, R. K. Schlenker, R. B. Taylor, H. S. Tsai, M. F. van Leeuwen, J. Webjorn, M. Ziari, D. Perkins, J. Singh, S. G. Grubb, M. S. Reffle, D. G. Mehuys, F. A. Kish, and D. Welch, "Large-scale photonic integrated circuits," *IEEE J. Sel. Topics Quantum Electron.*, vol. 11, no. 1, pp. 50–65, Jan./Feb. 2005.

[15] M. Smit, S. Oei, F. Karouta, R. Nötzel, J. Wolter, E. Bente, X. Leijtens, J. van der Tol, M. Hill, H. D. D. Khoe, and H. Binsma, "Photonic integrated circuits: Where are the limits?," in *Integr. Photon. Res. Applicat. Tech. Dig.*, San Diego, CA, Apr. 11–15, 2005, IWB1.

[16] H. Schmuck, "Comparison of optical millimeter-wave system concepts with regard to chromatic dispersion," *Electron. Lett.*, vol. 31, no. 21, pp. 1848–1849, 1995.

[17] M. K. Smit, "New focusing and dispersive planar component based on an optical phased array," *Electron. Lett.*, vol. 24, no. 7, pp. 385–386, 1988.

[18] J. H. den Besten, "Integration of multiwavelength lasers with fast electro-optical modulators," Ph.D. dissertation, Tech. Univ. Eindhoven, Eindhoven, The Netherlands, 2004.

[19] R. Krähenbühl, *Electro-Optic Space Switches in InGaAsP/InP for Optical Communication*, 2nd ed. Berlin, Germany: Springer-Verlag, 1998.

[20] D. Caprioli, J. H. den Besten, E. Smalbrugge, T. de Vries, X. J. M. Leijtens, M. K. Smit, R. van Dijk, F. E. van Vliet, W. Pascher, and J. J. M. Binsma, "A 10 Gb/s travelling wave MZ-modulator for integration with a laser," in *Proc. 11th Eur. Int. Opt. Conf.*, Prague, Czech Republic, Apr. 2–4, 2003, pp. 145–148.

[21] L. Mörl, D. Hoffmann, K. Matzen, C. Bornholdt, G. G. Mekonnen, and F. Reier, "Traveling wave electrodes for 50 GHz operation of opto-electronic devices based on InP," in *Proc. IPRM99 Conf.* , Davos, Switzerland, May 16–20, 1999, pp. 385–388.

[22] J. H. den Besten, D. Caprioli, R. van Dijk, F. E. van Vliet, W. Pascher, J. J. M. Binsma, E. Smalbrugge, T. de Vries, R. G. Broeke, Y. S. Oei, E. J. A. M. Bente, X. J. M. Leijtens, and M. K. Smit, "Integration of MZI modulators and AWG-based multiwavelength lasers in InP," in *Proc. IEEE/LEOS Symp.*, Ghent, Belgium, Dec. 2–3, 2004, pp. 95–98.

[23] F. M. Soares, F. Karouta, E. Smalbrugge, M. K. Smit, J. J. M. Binsma, J. Lopez, A. Enard, and N. Vodjdani, "An InP-based photonic integrated beamformer for phased-array antennas," in *Integr. Photon. Res. Tech. Dig.*, San Francisco, CA, Jun. 30–Jul. 2, 2004, IFB2.

[24] F. Soares, F. Karouta, E. Geluk, J. van Zantvoort, H. de Waardt, R. Baets, and M. Smit, "Low-Loss InP-based spot-size converter based on a vertical taper," in *Proc. 12th Eur. Int. Opt. Conf.*, Grenoble, France, Apr. 6–8, 2005, pp. 104–107.

[25] J. Galière, J. L. Valard, and E. Estèbe, "Millimeter-wave MMIC packaging compatible with surface-mount technology (SMT)," presented at the Eur. Microw. Conf., 2004.

[26] F. Xia, J. K. Thomson, M. R. Gokhale, P. V. Studenkov, J. Wei, W. Lin, and S. R. Forrest, "An asymmetric twin-waveguide high-bandwidth photodiode using a lateral taper coupler," *IEEE Photon. Technol. Lett.*, vol. 13, no. 8, pp. 845–847, Aug. 2001.

[27] Y. Miyamoto, M. Yoneyama, Y. Imai, K. Kato, and H. Tsunetsugu, "40 Gbit/s optical receiver module using a flip-chip bonding technique for device interconnection," *Electron. Lett.*, vol. 34, no. 5, pp. 493–494, 1998.

[28] "Final Project Rep.," OBANET, Proj. Deliverable D1.2.

[29] P. Sanchis, V. Polo, J. Herrera, J. L. Corral, M.-S. Choi, and J. Martí, "Experimental demonstration of a direction of arrival estimation algorithm for millimeter-wave switched-beam array antennas," *Microw. Opt. Technol. Lett.*, vol. 39, pp. 199–201, Aug. 2003.

[30] P. Sanchis, P. Sanchis, V. Polo, J. Herrera, J. L. Corral, M. Choi, and J. Marti, "Experimental demonstration of a direction of arrival estimation algorithm for mm-wave broad-band communication systems," in *IEEE MTT-S Int. Microw. Symp. Dig.*, Philadelphia, PA, Jun. 2003, pp. 1534–1536.

Miguel A. Piqueras, photograph and biography not available at time of publication.

Gerd Grosskopf, photograph and biography not available at time of publication.

Borja Vidal, photograph and biography not available at time of publication.

Javier Herrera, photograph and biography not available at time of publication.

Jose Manuel Martínez, photograph and biography not available at time of publication.

Pablo Sanchis, photograph and biography not available at time of publication.

Valentín Polo, photograph and biography not available at time of publication.

Juan. L. Corral, photograph and biography not available at time of publication.

Alexandre Marceaux, photograph and biography not available at time of publication.

Julien Galière, photograph and biography not available at time of publication.

Jérôme Lopez, photograph and biography not available at time of publication.

Alain Enard, photograph and biography not available at time of publication.

Jean-Luc Valard, photograph and biography not available at time of publication.

Olivier Parillaud, photograph and biography not available at time of publication.

Eric Estèbe, photograph and biography not available at time of publication.

Nakita Vodjdani, photograph and biography not available at time of publication.

Moon-Soon Choi, photograph and biography not available at time of publication.

Jan Hendrik den Besten, photograph and biography not available at time of publication.

Francisco M. Soares, photograph and biography not available at time of publication.

Meint K. Smit, photograph and biography not available at time of publication.

Javier Marti, photograph and biography not available at time of publication.